Computers & Geosciences 103 (2017) 80–91

Contents lists available at ScienceDirect

Computers & Geosciences

journal homepage: www.elsevier.com/locate/cageo

Research paper

EdgeDetectPFI: An algorithm for automatic edge detection in potential field anomaly images – application to dike-like magnetic structures

Saulo P. Oliveira[a,*], Francisco J.F. Ferreira[b], Jeferson de Souza[c]

[a] Federal University of Paraná, Department of Mathematics, Curitiba-PR, Brazil
[b] Federal University of Paraná, Department of Geology, Laboratory for Research in Applied Geophysics, Curitiba-PR, Brazil
[c] Paraná State Secretary of Education, Curitiba-PR, Brazil

ARTICLE INFO

Keywords:
Edge detection
Aeromagnetometry
Signum transform

ABSTRACT

We propose an algorithm to automatically locate the spatial position of anomalies in potential field images, which can be used to estimate the depth and width of causative sources. The magnetic anomaly is firstly enhanced using an edge detection filter based on a simple transformation (the Signum transform) which retains only the signs of the anomalous field. The theoretical edge positions can be recognized from the locations where one of the spatial field derivatives (or a function of them) change its sign: the zero crossover points. These points are easily identified from the Signum transformed spatial derivatives. The actual sources depths and widths are then estimated using the widths of the positive plateaus obtained from two different Signum transformed data: one based on the vertical derivative and the other using the vertical derivative minus the absolute value of the horizontal derivative. Our algorithm finds these widths in an automatic fashion by computing the radius of the largest circles inside the positive plateaus. Numerical experiments with synthetic data show that the proposed approach provides reliable estimates for the target parameters. Additional testing is carried out with aeromagnetic data from Santa Catarina, Southern Brazil, and the resulting parameter maps are compared with Euler deconvolution.

1. Introduction

Several methods have been proposed to estimate the location of potential field sources from gravimetric and magnetic data. In particular, methods based on field derivatives are easy to implement and demand a low computational effort, such as the tilt angle (Miller and Singh, 1994; Verduzco et al., 2004), the Theta map (Wijns et al., 2005), the normalized horizontal tilt angle (TDX) (Cooper and Cowan, 2006), and the tilt angle of the horizontal gradient (TAHG) (Ferreira et al., 2013).

Besides spatial locations, source depths are useful in the interpretation of magnetic anomalies. Usually, interpretation is carried out assuming sources with simple geometries, such as dike-like models which suits many geological situations (Ram Babu et al., 1986).

Based on the fact that the theoretical edges of the sources can be recognized from the locations where one or more of the spatial derivatives change sign, De Souza and Ferreira (2012) proposed a simple derivative-based filter, namely the *Signum transform*, where these derivatives are normalized in order that only their signs (+1 or −1) are retained. They showed that, for a dike-like model, the points where the sign changes, i.e, the zero-crossover points, do not exactly coincide with the true edge location, and formulas for calculating the exact edge positions and depths for vertically magnetized dike-like sources were developed. We remark that interpretation methods based on locating the zero-crossover points of potential field derivatives have previously been proposed in the literature (McGrath, 1991).

The formulas found in De Souza and Ferreira (2012) depend on the distances from the center of the sources to the zero-crossover points of the Signum-transformed derivatives. Finding such distances from a single 2D magnetic anomaly is straightforward (de Souza and Ferreira, 2013), but becomes challenging in the case of 3D data. In this work we propose an algorithm that produces a map of these distances by computing the radius of the largest circles within the anomalies (where the Signum transform equals 1), from which the formulas can be

* Corresponding author.
E-mail addresses: saulopo@ufpr.br (S.P. Oliveira), francisco.ferreira@ufpr.br (F.J.F. Ferreira), jdesouza@ufpr.br (J.d. Souza).

http://dx.doi.org/10.1016/j.cageo.2017.02.006
Received 26 May 2016; Received in revised form 8 February 2017; Accepted 11 February 2017
Available online 10 March 2017
0098-3004/

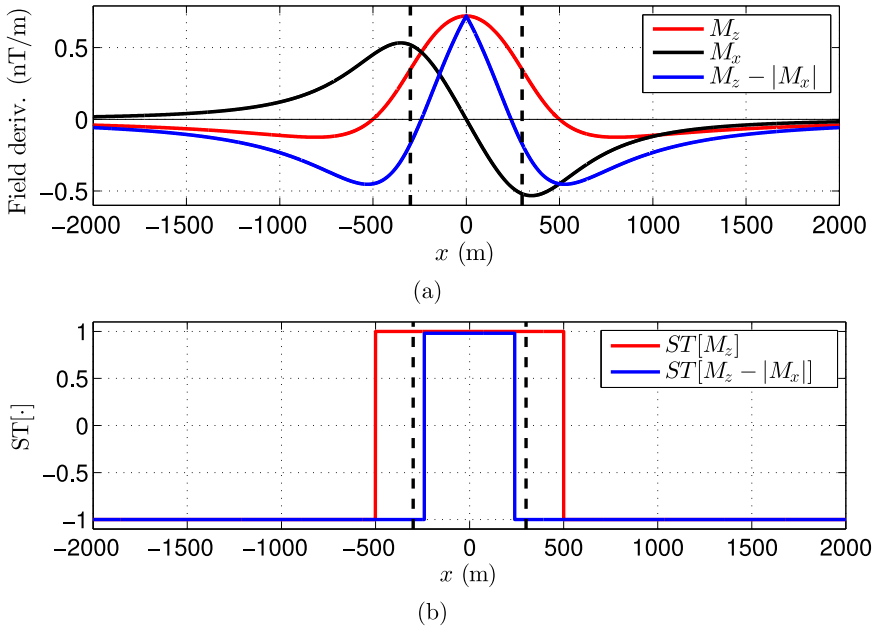

Fig. 1. Field derivatives M_z and $Mz - |M_x|$ (a) and their (dimensionless) Signum transforms (b) corresponding to the anomaly given by Eq. (2) with h=400 m and a=300 m. The vertical lines in black are $x = \pm a$.

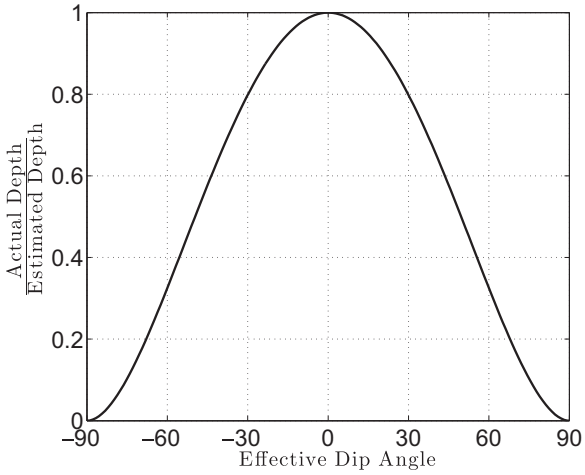

Fig. 2. Ratio of the actual depth to the estimated depth according to Eq. (12) plotted against the effective dip angle Q for a non-vertical magnetization.

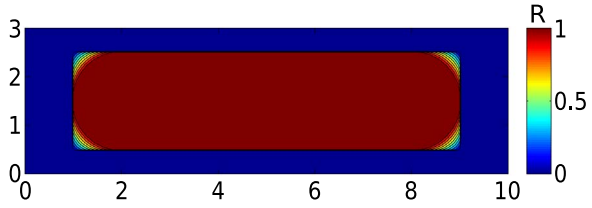

Fig. 4. Final result of the algorithm applied to a thin rectangle. The distances are, almost everywhere, the height of the rectangle, as it would be expected from a rectangle with infinite length.

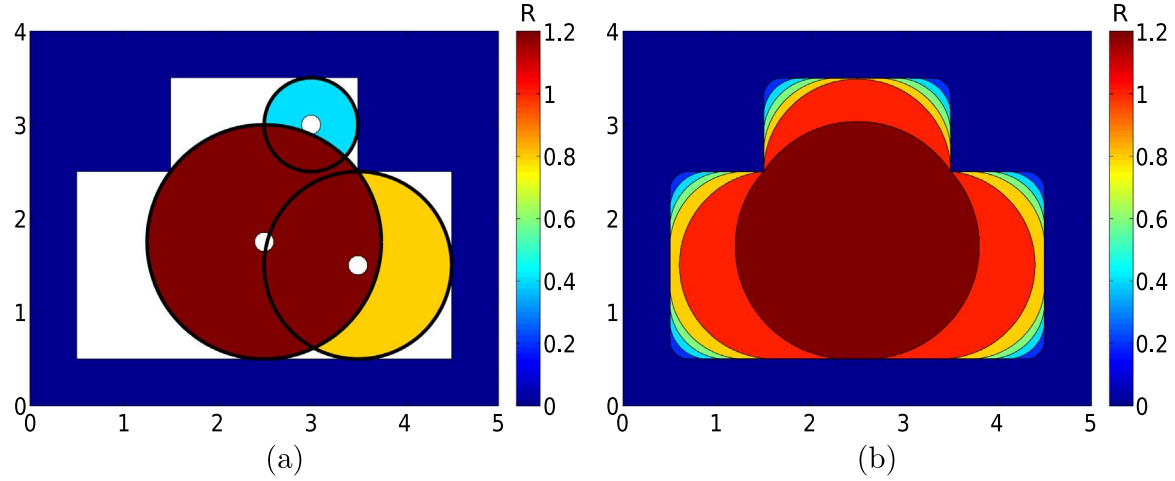

Fig. 3. (a): Largest inscribed circles produced by the algorithm from the three points marked in white. The colorbar indicates the radii of these circles in units of length. The white polygon contains the grid points (x_i^+, y_i^+) such that S_i=+ 1. At the points where the circles overlap, the radius of the larger circle (in brown) prevails. (b): final result of the algorithm, after all points in the polygon have been scanned.

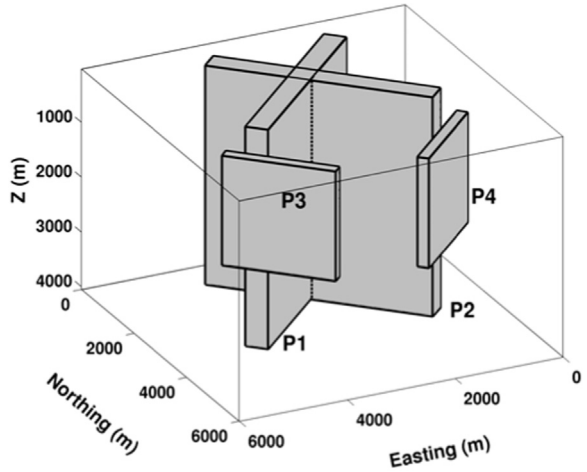

Fig. 5. Synthetic 3D model of four prisms (their attributes are presented in Table 1).

evaluated in an automatic fashion.

In the following, we review the underlying theory of the Signum transform method and present the distance-finding algorithm. Afterwards, we evaluate our approach using a synthetic model. We also apply the algorithm to aeromagnetic data acquired in the State of Santa Catarina, Southern Brazil.

2. Theory

We define the Signum transform of a function f as follows:

$$ST[f(x, y, z)] = \begin{cases} \dfrac{f(x, y, z)}{|f(x, y, z)|}, & f(x, y, z) \neq 0, \\ 1, & f(x, y, z) = 0. \end{cases} \quad (1)$$

Herein, x, y, and z denote spatial coordinates. A similar definition holds if $f = f(x)$ or $f = f(x, y)$. When $f = M_z = \partial M/\partial z$, where M is the magnetic anomaly, the values of $ST[f]$ are expected to be 1 over the sources and −1 out of them, providing the sources outcrop and have vertical magnetization. Thus, the sources are represented by plateaus where the value of the filtered anomalies is +1. However, the calculated boundaries are displaced from the real ones, especially for deep sources, making the bodies appear larger than they are.

2.1. Vertical magnetization

The vertical derivative of a magnetic anomaly due to a vertical dike of infinite length and depth extent located at the magnetic pole, with induced magnetization only, is

$$M_z(x, z)|_{z=0} = 2A\frac{a(a^2 + h^2 - x^2)}{(a^2 + 2ax + x^2 + h^2)(a^2 - 2ax + x^2 + h^2)}, \quad (2)$$

where a is one-half of dike width and h is depth to top of the dyke. The amplitude factor A is given as

$$A = 2Jbc\sin\theta,\ b = \sqrt{\sin^2 i + \cos^2 i\cos^2 d},\ c = \sqrt{\sin^2 I + \cos^2 I\cos^2 D}, \quad (3)$$

where J is the total magnetization intensity, θ is the geological dip of the dike, (i,d) are the inclination and declination of the resultant magnetization, and (I,D) are the inclination and declination of the Earth's magnetic field (Barongo, 1985; Radhakrishna Murthy, 1985). For a strictly vertical anomalous field, we have $A = 2J$.

The points x_v such that $M_z = M_z(x, 0) = 0$ are given as

$$x_v = \pm\sqrt{a^2 + h^2}. \quad (4)$$

Because Eq. (4) has two parameters, an additional equation must be provided to determine both a and h. The x-derivative

$$M_x(x, z)|_{z=0} = 2A\frac{-2ahx}{(a^2 + 2ax + x^2 + h^2)(a^2 - 2ax + x^2 + h^2)}, \quad (5)$$

vanishes at x=0, i.e., its root does not depend on a or h. In contrast, the roots of $M_z - |M_x|$ are given as

$$x_{vh-} = \pm\,(h - \sqrt{a^2 + 2h^2}). \quad (6)$$

Fig. 1 shows the derivatives and their Signum transforms. Note that we can readily find the crossover points x_v and x_{vh-} from the Signum transforms. Note also that the theoretical edge locations provided by x_v and x_{vh-} do not correspond to the actual ones.

2.2. Non-vertical magnetization

For non-vertical magnetization, Eqs. (2)–(5) have an additional parameter, as shown below:

$$M_z(x, z)|_{z=0} = 2A\frac{a(a^2 + h^2 - x^2)\cos Q + 2ahx\sin Q}{(a^2 + 2ax + x^2 + h^2)(a^2 - 2ax + x^2 + h^2)}, \quad (7)$$

$$M_x(x, z)|_{z=0} = 2A\frac{-2ahx\cos Q + a(a^2 + h^2 - x^2)\sin Q}{(a^2 + 2ax + x^2 + h^2)(a^2 - 2ax + x^2 + h^2)}, \quad (8)$$

where the parameter $Q = \lambda + \psi - \theta(\tan\lambda = \tan I/\cos D,\ \tan\psi = \tan i/\cos d)$ is the effective dip angle. In this case the curve for the derivatives become asymmetrical and the crossovers points are laterally displaced toward the effective dip direction vector. The crossover points for these cases are

$$x_v = hk \pm \sqrt{a^2 + h^2k^2 + h^2}, \quad (9)$$

Table 1
Parameters of the prisms in the synthetic example.

Parameters	P1	P2	P3	P4
Width (m)	400	400	200	200
Length (m)	4000	4000	2000	2000
Thickness (m)	4000	4000	2000	2000
Depth to top (m)	50	50	200	300
Azimuth (deg)	45	−45	−45	45
Magnetic susceptibility (SI)	0.027	0.027	0.027	0.027
x-coordinate of center (m)	3000	2500	4500	1500
y-coordinate of center (m)	2000	2000	4500	4500

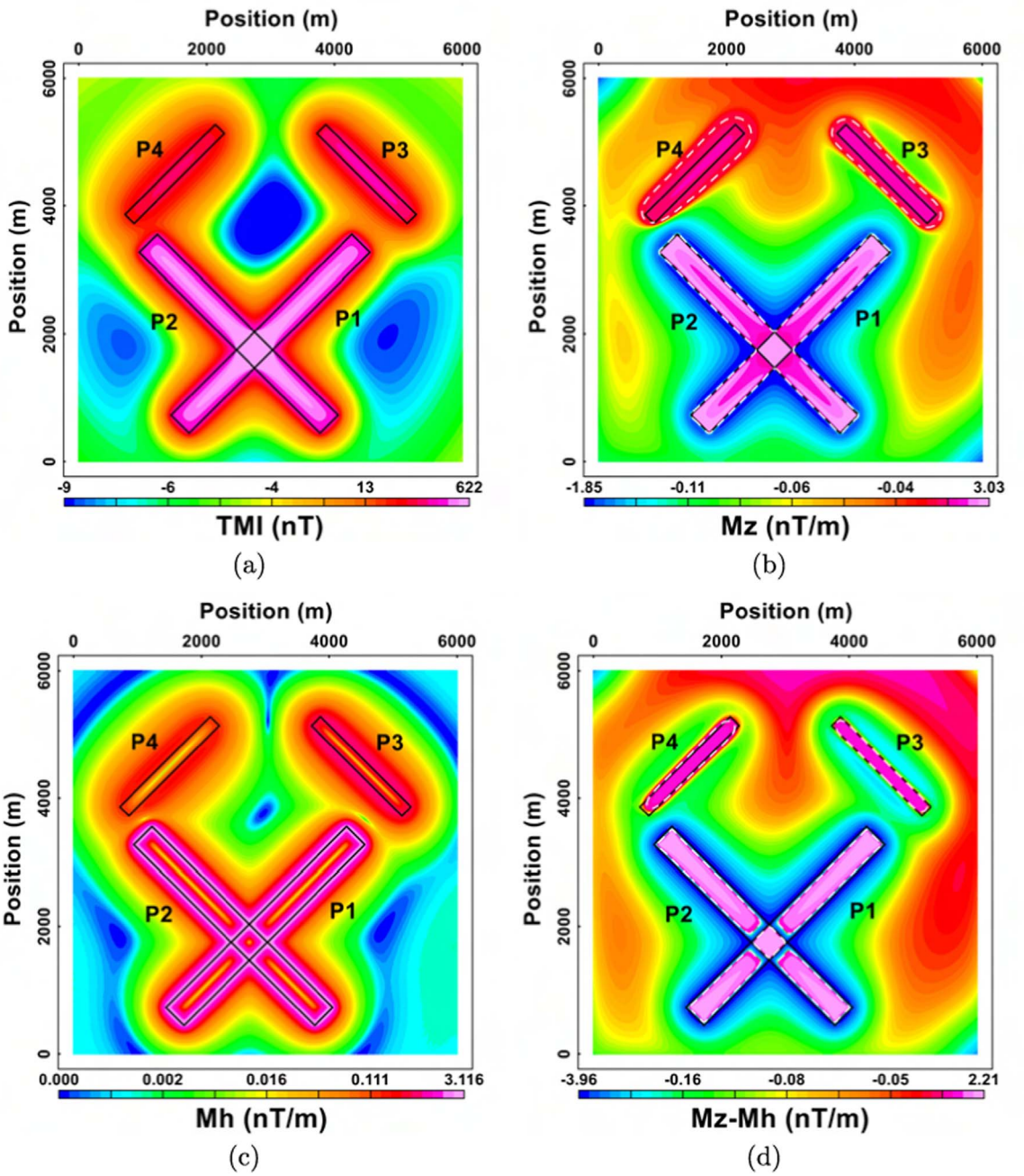

Fig. 6. (a) Total Magnetic Intensity (TMI) map of the synthetic model shown in Fig. 5. (b) Vertical derivative (M_z) of the data in (a). (c) Total horizontal derivative (M_h) of the data in (a). (d) Vertical derivative minus total horizontal derivative ($M_z - M_h$) of the data in (a). White, dashed lines in (b) and (d) indicate the zero-crossover points of the derivatives.

$$x_{vh} = \frac{-h + \sqrt{a^2k^2 \pm 2a^2k + a^2 + 2h^2k^2 + 2h^2} \pm hk}{k \pm 1}, \qquad k = \tan Q. \tag{10}$$

Note that Eqs. (9)–(10) tend to Eqs. (4)–(6) as k tends to 0. Thus, for small k-values, Eqs. (4)–(6) are still valid in an approximate fashion. The parameter k will be small if the remanent field is weak and/or the orientation of the remanent field does not deviate too much from the Earth's magnetic field direction. If these conditions are not satisfied, the algorithm can still be applied since the k parameter can be obtained. For instance, one can estimate k using Eq. (6) of Radhakrishna Murthy (1985):

$$k = \frac{M_x(x_{center}, 0)}{M_z(x_{center}, 0)}, \tag{11}$$

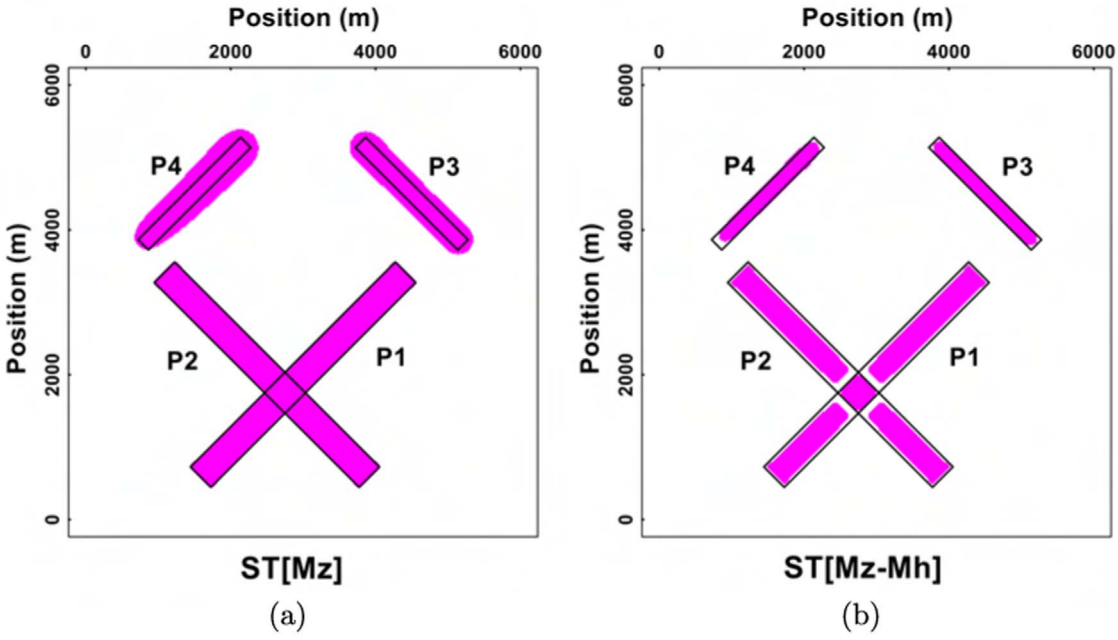

Fig. 7. Signum transforms of M_z (a) and $M_z - M_h$ (b), with $M_h^2 = M_x^2 + M_y^2$.

where x_{center} are the centers of the causative bodies. These points could be located by finding the extreme points of analytic signal amplitude (ASA) anomalies, whose positions are independent on the magnetic dip direction. This subject will be addressed in a forthcoming work.

3. Material and methods

3.1. Theoretical estimates for depth and width

In the previous section we derived relations between zero-crossover points x_v and x_{vh-} and dike parameters a and h. De Souza and Ferreira (2012) proposed theoretical estimates for these parameters by combining Eqs. (4) and (6) to determine both a and h using x_v and x_{vh-} as input parameters:

$$h = \frac{x_v^2 - x_{vh-}^2}{2x_{vh-}}, \tag{12}$$

$$a = \sqrt{x_v^2 - h^2}. \tag{13}$$

These formulas are exact under the assumptions of Section 2.1, and provide estimates of depth to top (h) and half-width (a) for dike-like sources. To take into account variations in the y direction in three-dimensional anomalies, they replaced M_x with the total horizontal derivative $M_h = \sqrt{M_x^2 + M_y^2}$.

In Fig. 2 we analyze the relative error in the depth estimation when using formula (12) for sources whose effective dip angle Q is not zero, i.e., when the crossover points are represented by Eqs. (9) and (10) instead of (4) and (6). The relative error is lower than 45% for $|Q| < 45°$, and lower than 20% for $|Q| < 30°$. For $|Q| \approx 90°$, the error is very large and the method cannot be applied. The effective dip angle can vary from −540° to 180° (Ram Babu et al., 1986), but the curve will repeat itself on the interval below −90° and above 90°. Thus the method will be valid in an approximate fashion for effective dip angles near $\pm n \times 90°$ when n is even, but it will be inaccurate for odd values of n.

3.2. Algorithm

In this section we introduce the algorithm that finds x_v and x_{vh-}. We assume that the grid points (x_i, y_i), $1 \le i \le n$, are given in the arrays $\boldsymbol{x}$ and $\boldsymbol{y}$, as well as an array $\boldsymbol{S}$ is provided with the Signum transform of M_z or $M_z - |M_h|$ at these grid points. Specifically, $S_i = ST[M_z(x_i, y_i)])$ and $S_i = ST[(M_z - |M_h|)(x_i, y_i)]$ for $1 \le i \le n$ when we compute x_v and x_{vh-}, respectively. The parameter n is the number of points in the dataset.

The goal is to produce a map of largest inscribed circles in the region $S^+ = \{(x_j, y_j) \,|\, S(x_j, y_j) = +1\}$. The output vector $\boldsymbol{R}$ ($R_i = x_v(x_i, y_i)$ or $R_i = x_{vh-}(x_i, y_i)$) will be given by the values of this map at the grid points.

We split the grid points in two sets: the set $\{\boldsymbol{x}^+, \boldsymbol{y}^+\}$ with points (x_i^+, y_i^+) such that $S_i = +1 (1 \le i \le n^+)$, and the set $\{\boldsymbol{x}^+, \boldsymbol{y}^+\}$ with points (x_i^-, y_i^-) such that $S_i = -1 (1 \le i \le n^-)$.

The first step is to set $R_i = 0$ for any $1 \le i \le n$. Afterwards, for each (x_i^+, y_i^+) in $\{\boldsymbol{x}^+, \boldsymbol{y}^+\}$ we find the largest circle C_i, with center in (x_i^+, y_i^+) and radius r_i, such that $S_j = +1$ at any grid point (x_j, y_j) in the circle. We impose $R_j = r_i$ for any $(x_j^+, y_j^+) \in C_i$, unless $R_j \ge r_i$. An example of this step is shown in Fig. 3 a where three circles overlap. Denoting the largest circle as C_{i^*}, we have $R_j = r_{i^*}$ for all points (x_j, y_j) in C_{i^*}, even those belonging to the other two circles.

In order to determine r_i, we can build a vector with the distances d_j from (x_i^-, y_i^-) to each point (x_j^+, y_j^+) in $\{\boldsymbol{x}^-, \boldsymbol{y}^-\}$. Then, any circle centered in (x_i^-, y_i^-) with radius $r < \min\{\boldsymbol{d}\}$ will not contain grid points from $\{\boldsymbol{x}^-, \boldsymbol{y}^-\}$. We select $r_i = \min\{\boldsymbol{d}\} - \epsilon$, where $\epsilon > 0$ is half the grid size.

From this procedure we have that $\boldsymbol{R}$ is nearly constant for thin rectangular (prismatic) bodies, as expected (Fig. 4).

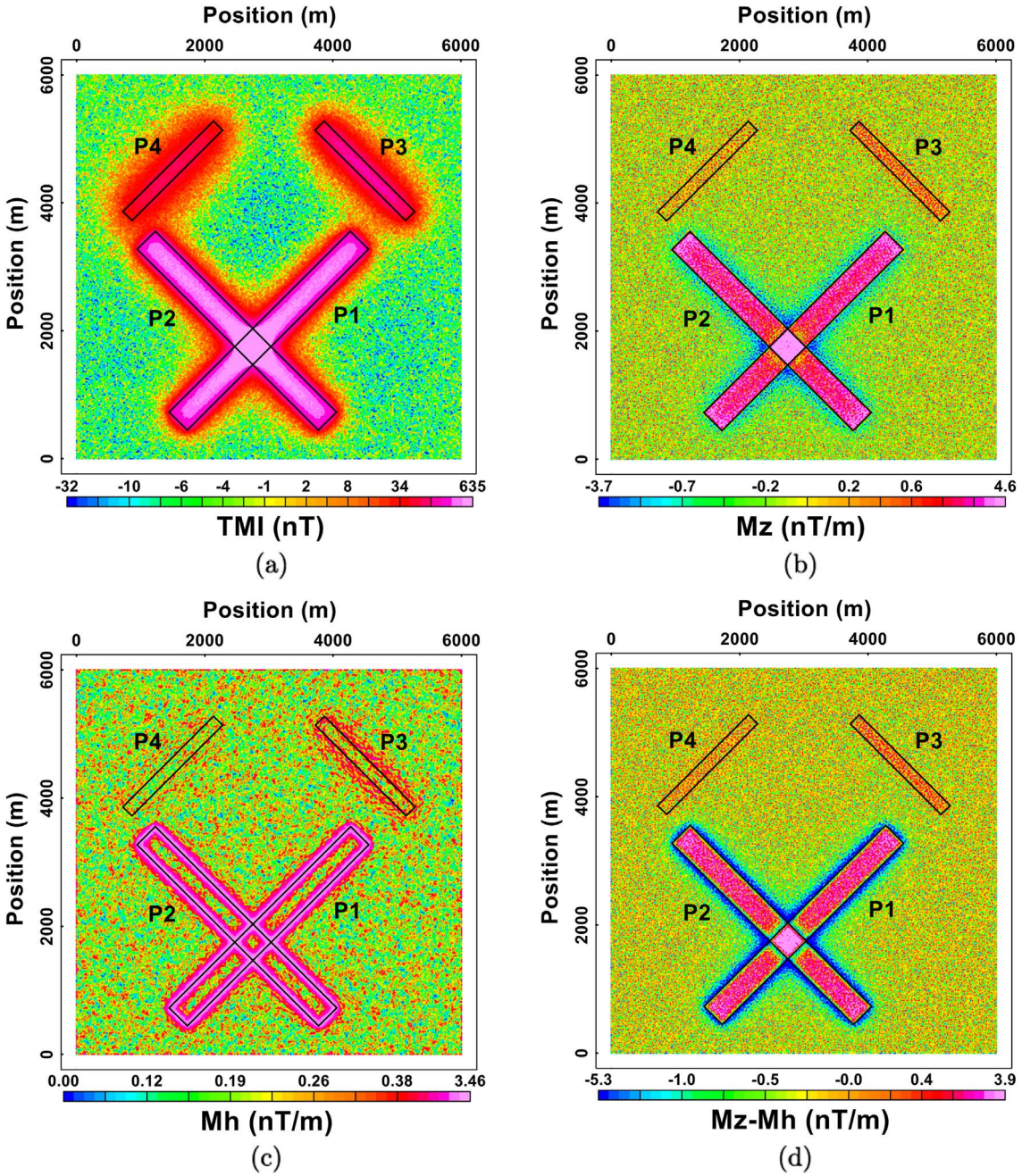

Fig. 8. (a) Total Magnetic Intensity (TMI) map of the synthetic model shown in Fig. 5 contaminated with Gaussian noise with 1% of maximum amplitude. (b) Vertical derivative (M_z) of the data in (a). (c) Total horizontal derivative (M_h) of the data in (a). (d) Vertical derivative minus total horizontal derivative ($M_z - M_h$) of the data in (a). White, dashed lines in (b) and (d) indicate the zero-crossover points of the derivatives.

Algorithm 1. Largest incribed circles in the region where $S(x, y) = 1$.

Input data: $\boldsymbol{x}$, $\boldsymbol{y}$, $\boldsymbol{S}$, and ϵ;
Find $\{\boldsymbol{x}^-, \boldsymbol{y}^-\}$ and $\{\boldsymbol{x}^+, \boldsymbol{y}^+\}$;
$R_i \leftarrow 0, 1 \le i \le n$;
for $i \leftarrow 1, \ldots, n^+$ **do**
  $R_i \leftarrow 0, 1 \le i \le n$;
  $d_j \leftarrow \|(x_i^+, y_i^+) - (x_j^-, y_j^-)\|, 1 \le j \le n^-$;
  $r_i \leftarrow \min\{\boldsymbol{d}\} - \epsilon$;
  for $j \leftarrow 1, \ldots, n^+$ **do**
    if $\|(x_i^+, y_i^+) - (x_j^+, y_j^+)\| \le r_i$ **then**
      $R_j \leftarrow \max\{R_j, r_i\}$;
    end if
  end for
end for

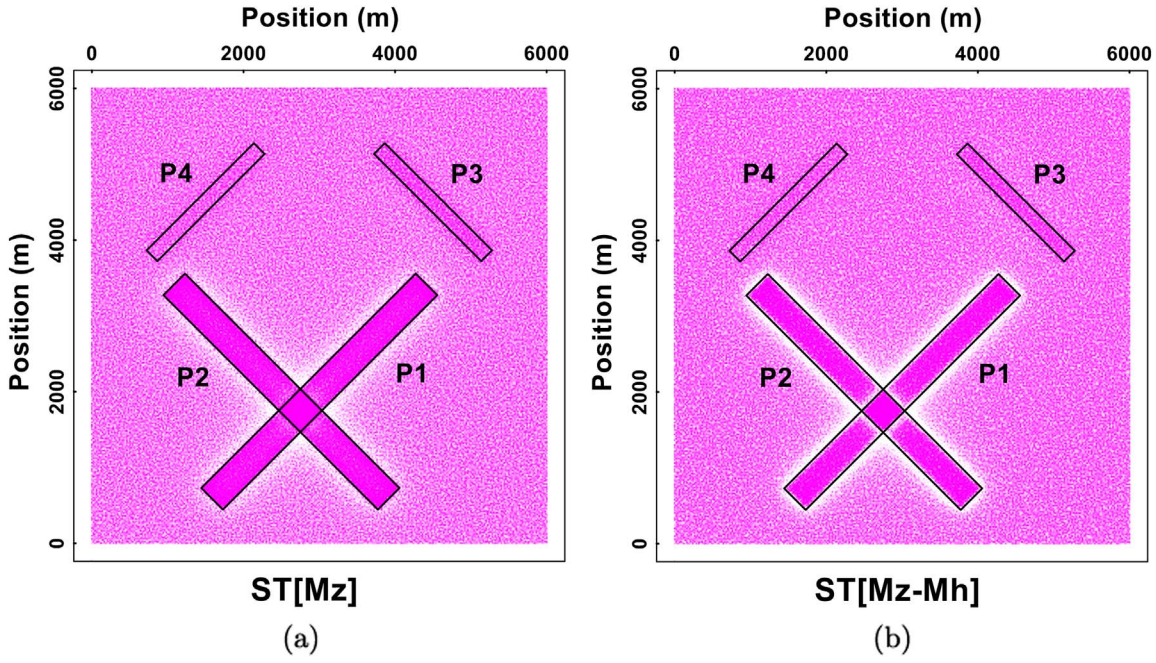

Fig. 9. Signum transforms of M_z (a) and $M_z - M_h$ (b), with $M_h^2 = M_x^2 + M_y^2$. The magnetic anomaly was contaminated with Gaussian noise with 1% of maximum amplitude.

For simplicity, we provide in Algorithm 1 a pseudo-code implementation in sequential form of the proposed technique. Regarding computational cost, the calculation of $\boldsymbol{d}$, r_i, and $\boldsymbol{R}$ at each step i ($1 \le i \le n^+$) requires $\boldsymbol{O}(n^-)$, $\boldsymbol{O}(n^-)$, and $\boldsymbol{O}(n^+)$ operations, respectively, so the algorithm complexity is roughly $\boldsymbol{O}(n^2)$. On the other hand, the classical Euler deconvolution method (Thompson, 1982) with a window of N_w grid points requires solving least-squares systems of size $N_w \times 3$ for each interior grid point. Assuming $N_w \ll n$, we have an algorithm complexity of $\boldsymbol{O}(n)$. Despite the fact Algorithm 1 has a higher complexity, the processing time is substantially reduced when implemented in vector form. A vectorized source code in language Fortran 90 is available at https://github.com/cageo/.

4. Results and discussion

In the following we apply the EdgeDetectPFI algorithm to synthetic and real data. A Fortran 90 implementation of the algorithm has been executed in a desktop computer with 16 Gb RAM and a 3.6 GHz Intel Core i7-4790 processor.

4.1. Synthetic anomaly model

Let us consider the synthetic model shown in Fig. 5, composed of four prisms, whose parameters are presented in Table 1. All prisms satisfy the criterion for two-dimensionality, i.e., the bodies strike length is at least 10–20 times the other dimensions (Telford et al., 1990, p. 39,95). Fig. 6 shows the synthetic magnetic anomalies and their derivatives at the magnetic pole, with induced magnetization only, which have been generated with the open-source code Grav_Mag_Prism (Bongiolo et al., 2013) with grid cell size of 20 m .

Afterwards, the magnetic anomaly was contaminated with Gaussian noise with a standard deviation equal to 1% of maximum data amplitude. The effect of the noise on the magnetic anomaly and its derivatives is shown in Fig. 8.

The Signum transform of the derivatives are shown in Fig. 9. Because Signum transform accounts for sign changes rather than amplitudes, even low-amplitude oscillations affect the ST maps, hence this transform is very sensitive to noise.

The computer code mentioned in the previous section uses the Signum transforms of M_z and $M_z - M_h$ (Fig. 7) to evaluate x_υ and x_{vh-}, which are then used in the calculation of h and a according to Eqs. (12)–(13). The CPU time spent by the code was 5.028 s (5.238 s for noisy data).

Fig. 10a and b present the estimated depth to top and width calculated from the Signum transforms shown in Fig. 7. Note that the estimated depths and widths are affected by interference between different sources, which is apparent in the intersection between prisms P1 and P2.

Parameters estimation for deeper prisms P3 and P4 are less resolved than the shallower prisms P1 and P2, besides being affected by the their fields which distort the apparent width, leading to errors in the estimation of the true widths and depths. Nevertheless, predicted widths and depths are close to the true values presented in Table 1.

Figs. 10c and d show the estimated parameters for the synthetic data contaminated with Gaussian noise (Fig. 8). These results indicate that estimates Eqs. (12) and (13) are also very sensitive to noise, and the locations of prisms P3 and P4 are not easily identified. The presence of shallow, thick prisms and deep, thin prisms led to huge differences in anomaly amplitude. The maximum amplitude generated at the intersection between the two longer prisms is about 20 times greater than the maximum amplitude of the smaller, deep ones. Thus 1% of the maximum anomaly amplitude corresponds to approximately 20% of the amplitude of those smaller prisms. Thus, magnetic data with large amplitude variation (due to highly inhomonogeneous

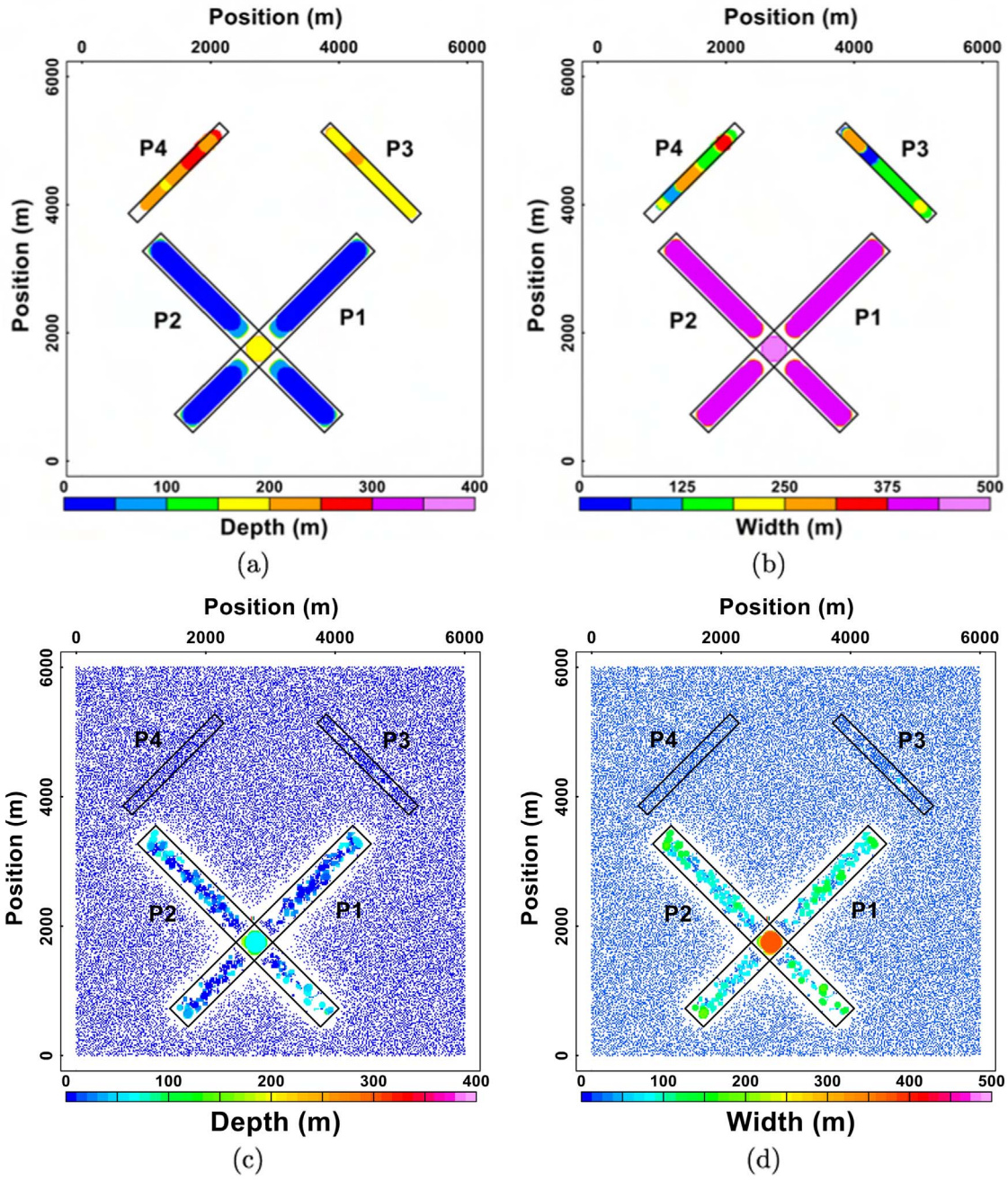

Fig. 10. Depth to top (a) and width (b) of the prisms estimated from the Signum transforms based on Eqs. (12)–(13). In Figures (c) and (d), the anomaly map was contaminated with Gaussian noise with 1% of maximum amplitude.

sources characteristics) should be pre-processed with a denoising technique prior to using our algorithm. In the next section we will use upward continuation to attenuate the noise.

4.2. Potential field data

In this section we consider aeromagnetic field data from southern Brazil. The study area covers 27.8 km by 27.8 km, and has three main geological unities (Basei et al., 2011a), namely the Brusque Group, Itajaí Group and Paleoproterozoic Basement (Fig. 11).

These unities are within the Dom Feliciano orogenic belt which is related to the interation of Rio de la Plata and Kalahari Cratons during the Brasiliano/Pan-Africano cycle in south Brazil and Uruguay (de Campos et al., 2012).

The Brusque Group (940–840 Ma) consists of acid metavolcanic rocks intercalated with metasedimentary sequence. It represents an orogenic segment of Brasiliano age (Basei et al., 2011a; de Campos et al., 2012). Intrusive diabase dikes oriented N45°E, related to post-

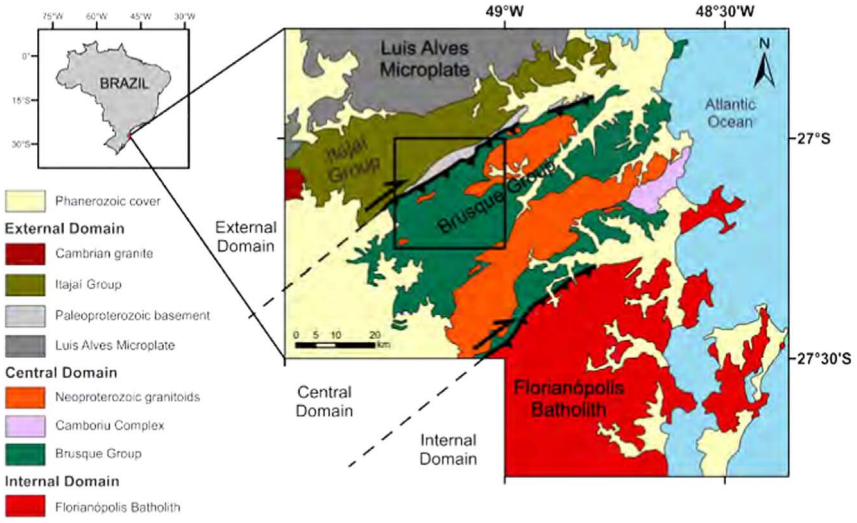

Fig. 11. Tectonic map of the Dom Feliciano Belt, State of Santa Catarina, southern Brazil. The study area is indicated by the square frame (adapted from Basei et al. (2011a)).

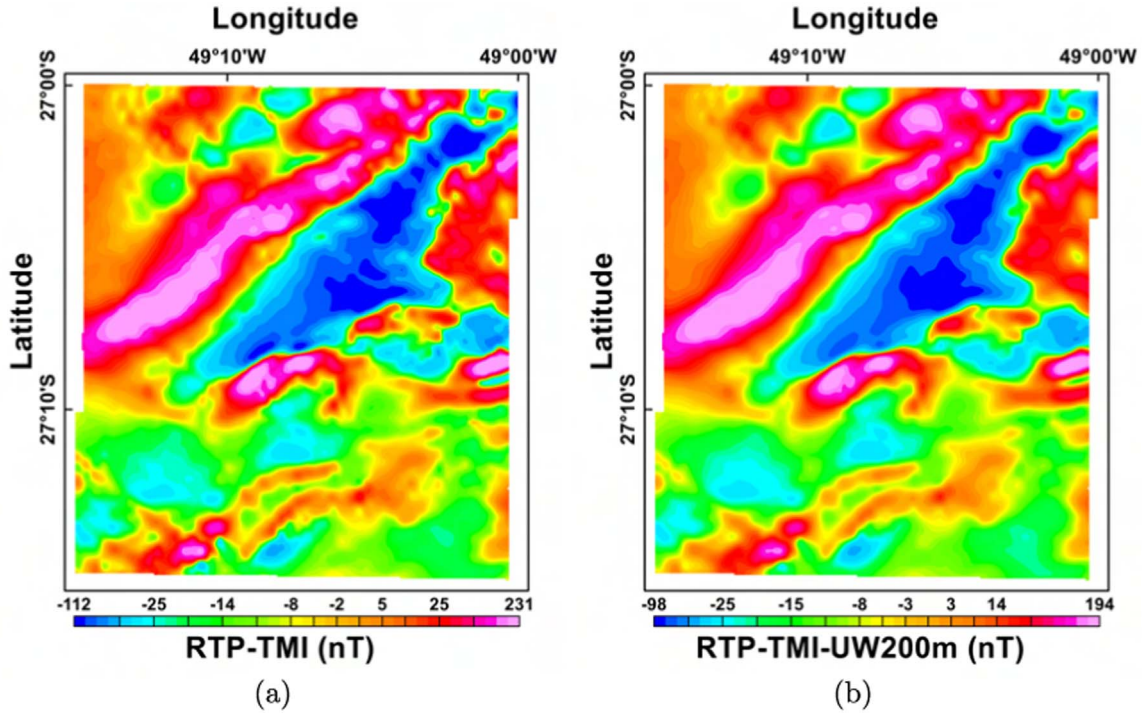

Fig. 12. RTP-TMI map of the magnetic anomalies shown in the inset of Fig. 11 (a) and RTP-TMI calculated from the same magnetic anomalies upward continued to 200 m (b).

colisional magmatism of the Brasiliano orogeny have been identified by geological studies (de Campos et al., 2012).

The collision-related Itajaí foreland basin consists of metamorphosed siliciclastic sediments of alluvial, deltaic and marine origin, and the upper parts are filled by Precambrian turbiditic deposits. It represents a record of the Ediacaran period. According to Basei et al. (2011b), the Itajaí Basin started around 600 Ma, with deposition on the gneisses of the Luís Alves Microplate southern border (Fig. 11). The sedimentation ceased around 560 Ma, as attested by the existence of felsic dikes and domes crosscutting the sedimentary sequence

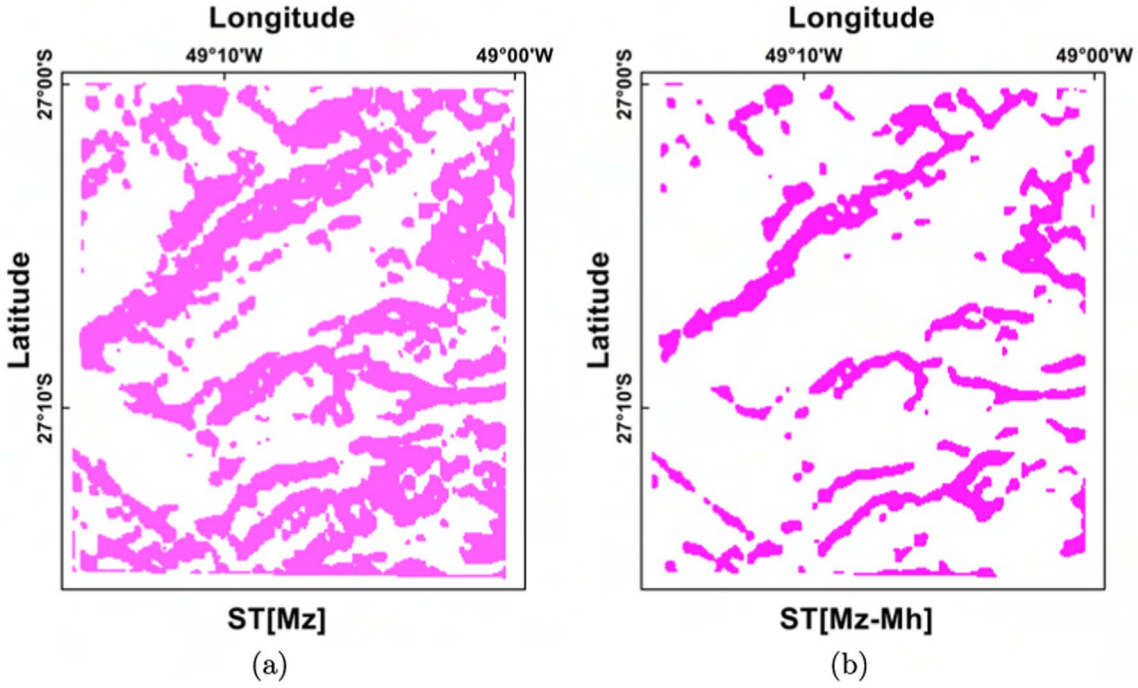

Fig. 13. Signum transforms of M_z (a) and $M_z - M_h$ (b), with $M_h^2 = M_x^2 + M_y^2$, from data shown in Fig. 12b.

(Rostirolla et al., 1999; Basei et al., 2011b).

The aeromagnetic data of the Paraná-Santa Catarina Project were acquired by CPRM - Serviço Geológico do Brasil (2011) between 10 November 2009 and 11 July 2011, along north-south flight lines, spaced at 500 m, with a mean terrain clearance at 100 m. The tie lines spacing is 5 km.

The total magnetic intensity (TMI) data has a grid cell size of 100 m. The data have been reduced to the pole using a magnetic inclination of −37.05° and a declination of −18.17°, which corresponds to the magnetic field at the time of the airborne survey (Fig. 12a). The data have been upward continued to 200 m to reduce the noise (Fig. 12b). The reduced-to-the-pole (RTP) magnetic maps (Fig. 12) show strong northeast-southwest trend in the magnetic lineaments. The Signum transforms of M_z and $M_z - M_h$ are shown in Fig. 13.

We cannot ensure that all the linear anomalies in the magnetic map are caused by diabase dikes because their exact locations are not provided by the geological studies conducted in the area, such as de Campos et al. (2012). The width of the mapped dikes ranges from few meters to tens of meters and the main of them is about 750 m long and about 20–80 m wide (de Campos et al., 2012). Thus, the spatial resolution of the aeromagnetic survey (500 m spacing between flight lines) is lower than the widths of the geologically mapped magnetic bodies.

The depths of the sources, estimated from Eq. (12), are shown in Fig. 14, along with the depths estimated by Euler deconvolution (Thompson, 1982) dike model solutions, shown in Fig. 14b. Moreover, Fig. 14d shows the superposition of the depth maps shown in Figs. 14a and b. Fig. 14c shows the corresponding widths estimated from Eq. (13). The CPU time required for processing h and a was 6.995 s. For Euler deconvolution, we employed the structural index SI=1, window size 2000 m, and a tolerance of 3% for the estimated depth error.

One can notice from Fig. 14d that there are some lineaments whose estimated depths are similar in both Euler deconvolution and Signum transform methods. However, some structures identified in the Euler deconvolution method are not detected by Signum transform and vice versa. Therefore, the methods could be used as complementary interpretation tools. In general, depth estimation through Euler deconvolution provides deeper sources, although the highest depth values correspond to solutions that are not strongly clustered, which are likely to be spurious ones (Fig. 14b). It is worth mentioning that the Signum transform method yields a unique solution for the estimated depth, whereas Euler deconvolution depends on the appropriate choice of the above-mentioned parameters.

The general trends of the solutions in Figs. 14a–b are consistent with the general direction N45°E of the diabase dikes and the large regional structures (Fig. 11).

5. Conclusions

The algorithm introduced in this work is designed to identify linear patterns of images (in particular, potential fields) by locating the positive part of the signal, and measures the width of the patterns by finding the largest inscribed circles in the region where the signal is positive. We applied the algorithm to calculate the widths of the anomalies in the M_z and $M_z - |M_h|$ maps which have been subsequently used to estimate the true sources widths and depths. Rapid processing time and the comparison of the results with those from Euler deconvolution demonstrate the utility of the algorithm in the interpretation of magnetic anomalies. Despite the fact that the algorithm has been tested for magnetic data, for which the crossover-points have a physical meaning, it could be useful for any interpretation method that requires automatic evaluation of distances in contour data.

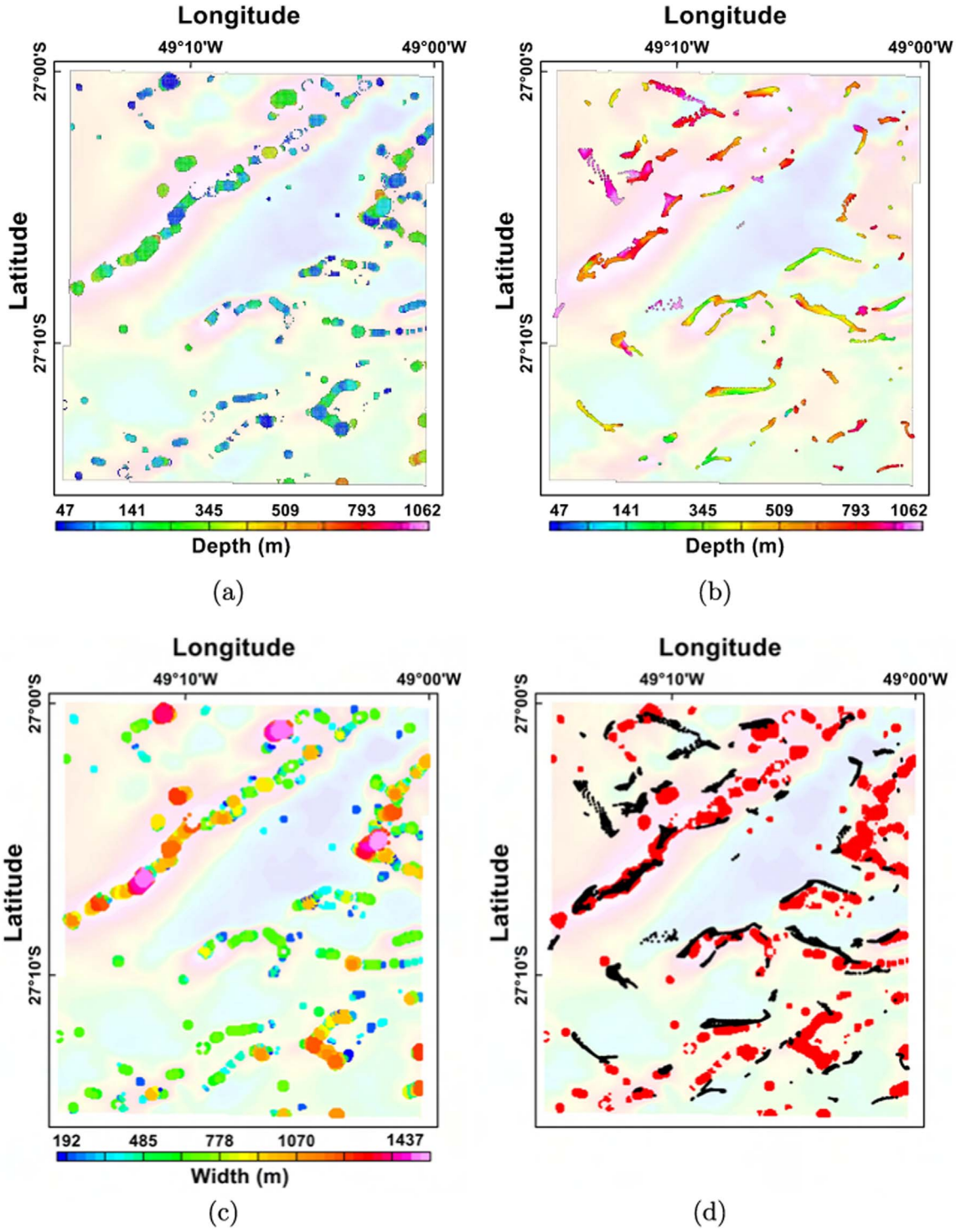

Fig. 14. Depth to top of the sources estimated from the Signum transform (a) and Euler deconvolution (b), and width of the sources estimated from the Signum transform (c) from data shown in Fig. 12b. Fig. 14d shows the superposition of Signum transform (red) and Euler deconvolution (black) solutions.

Acknowledgments

The authors thank Companhia de Pesquisa de Recursos Minerais (CPRM, Geological Survey of Brazil) for permission to use the aeromagnetic data, and Vinicius Antunes Ferreira da Silva for providing us with the tectonic map shown in Fig. 11. S. P. Oliveira is supported by CNPq under grant 306083/2014-0 and is a collaborator of INCT-GP. F. J. F. Ferreira and J. de Souza were supported in this research by CNPq and CAPES-Ciência sem Fronteiras Program, under contracts 306978/2015-6 and 10724-13-3, respectively.

References

Barongo, J.O., 1985. Method for depth estimation on aeromagnetic vertical gradient anomalies. Geophysics 50 (6), 963–968.

Basei, M., Neto, M.C., Castro, N., Nutman, A., Wemmer, K., Yamamoto, M., Hueck, M., Osako, L., Siga, O., Passarelli, C., 2011a. Tectonic evolution of the Brusque Group, Dom Feliciano belt, Santa Catarina, Southern Brazil. J. South Am. Earth Sci. 32 (4), 324–350.

Basei, M.A.S., Drukas, C., Nutman, A., Wemmer, K., Dunyi, L., Santos, P.R., Passarelli, C., Neto, M.C., Siga, O., Jr, Osako, L., 2011b. The Itajaí foreland basin a tectono-sedimentary record of the ediacaran period, Southern Brazil. Int. J. Earth Sci. 100 (2–3), 543–569.

Bongiolo, A., de Souza, J., Ferreira, F.J.F., de Castro, L.G., 2013. Grav mag prism: a matlab/octave program to generate gravity and magnetic anomalies due to rectangular prismatic bodies. Rev. Bras. Geof. 31 (3), 347–363.
de Campos, R.S., Philipp, R.P., Massonne, H.-J., Chemale, F., 2012. Early post-collisional brasiliano magmatism in Botuverá region, Santa Catarina, southern Brazil: evidence from petrology, geochemistry, isotope geology and geochronology of the diabase and lamprophyre dikes. J. South Am. Earth Sci. 37, 266–278.
Cooper, G.R.J., Cowan, D.R., 2006. Enhancing potential field data using filters based on the local phase. Comput. Geosci. 32 (10), 1585–1591.
CPRM - Serviço Geológico do Brasil, 2011. Aerogeophysical project Paraná-Santa Catarina: survey and processing of magnetometric and gamma-ray spectrometric data (in Portuguese).Tech. rep., Lasa Prospecções.
Ferreira, F.J.F., de Souza, J., Bongiolo, A., de Castro, L.G., 2013. Enhancement of the total horizontal gradient of magnetic anomalies using the tilt angle. Geophysics 78 (3), J33–J41.
McGrath, P.H., 1991. Dip and depth extent of density boundaries using horizontal derivatives of upward-continued gravity data. Geophysics 56 (10), 1533–1542.
Miller, H.G., Singh, V., 1994. Potential field tilt - a new concept for location of potential field sources. J. Appl. Geophys. 32 (2–3), 213–217.
Radhakrishna Murthy, I.V., 1985. Magnetic interpretation of dyke anomalies using derivatives. Pure Appl. Geophys. 123 (2), 232–238.
Ram Babu, H.V., Vijayakumar, V., Atchuta Rao, D., 1986. A simple method for the analysis of magnetic anomalies over dike-like bodies. Geophysics 51 (5), 1119–1126.
Rostirolla, S., Ahrendt, A., Soares, P., Carmignani, L., 1999. Basin analysis and mineral endowment of the Proterozoic Itajaíbasin, south-east Brazil. Basin Res. 11 (2), 127–142.
de Souza, J., Ferreira, F., J.F., 2012. On the use of derivatives for interpreting magnetic anomalies due to dyke-like bodies: Qualitative and quantitative analysis. In: Istanbul 2012 - International Geophysical Conference and Oil & Gas Exhibition. pp. 1–4.
de Souza, J., Ferreira, F.J.F., 2013. On the use of derivatives for interpreting magnetic anomalies due to dyke-like bodies II: application to synthetic and field data. In: 2013 SEG Annual Meeting. Society of Exploration Geophysicists, pp. 1121–1125.
Telford, W.M., Geldart, L.P., Sheriff, R.E., 1990. Applied Geophysics 2nd edition. Cambridge University Press.
Thompson, D.T., 1982. EULDPH a new technique for making computer-assisted depth estimates from magnetic data. Geophysics 47 (1), 31–37.
Verduzco, B., Fairhead, J.D., Green, C.M., MacKenzie, C., 2004. New insights into magnetic derivatives for structural mapping. Lead. Edge 23 (2), 116–119.
Wijns, C., Perez, C., Kowalczyk, P., 2005. Theta map edge detection in magnetic data. Geophysics 70 (4), L39–L43.